



RESEARCH ARTICLE

10.1002/2016RS006068

A new mode of radio wave diffraction via the terrestrial surface plasmon on mountain range

Masafumi Fujii¹¹Graduate Research Division of Science and Engineering, University of Toyama, Toyama, Japan**Key Points:**

- Surface plasmon is induced on the Earth's surface by radio waves in mountain ranges
- Radio wave interacts with the surface plasmon, causing anomalous diffraction and scattering at the ground roughness
- Radio wave can reach to distant locations beyond the line of sight by the surface plasmon on mountain peaks

Correspondence to:Fujii, M.
mfujii@eng.u-toyama.ac.jp**Citation:**Fujii, M. (2016), A new mode of radio wave diffraction via the terrestrial surface plasmon on mountain range, *Radio Sci.*, 51, 1396–1412, doi:10.1002/2016RS006068.

Received 30 APR 2016

Accepted 6 AUG 2016

Accepted article online 15 AUG 2016

Published online 24 AUG 2016

Abstract It is shown that a new mode of radio wave diffraction occurs at the peak of mountains mediated via the terrestrial surface plasmon. If mobile electrical charges exist on the Earth's surface, the electromagnetic theory predicts strong coupling between the radio wave and the surface plasmon on the ground. If sufficient amount of electrical charges of the same sign appear on the ground as a consequence of some underground preseismic activity, they will be subject to the electrical repulsive forces. The surface electrical charges will then move toward topographic highs of nearby mountain peaks. Radio waves are then shown to interact with such electrical charges and create collective oscillations of the surface charges to induce a surface plasmon. Here it is clarified with numerical analyses on a massively parallel supercomputer that such interactions occur on the peak of mountains, hence causing peculiar phenomena of random diffraction. Depending on the density of the electrical charges on the ground surface, the interaction becomes strong enough to cause intense and random scattering and diffraction of the radio wave from the rough surface of the mountain topography. Mountain peaks thus act as a secondary source of radio waves; unexpectedly, radio waves are reradiated from the peaks into various directions by the anomalous diffraction and scattering, and the reradiated wave can propagate beyond the line of sight over mountains to reach distant locations. Such effects may arise randomly but concurrently with some preseismic activity in the crustal rocks, of which observation may allow statistical analysis of the critical state of crustal rocks over a broad area of a few hundred kilometers.

1. Introduction

It has been theoretically shown that mobile electrical charges on the ground act as a surface plasma wave, or surface plasmon, and interact strongly with radio waves in the atmosphere [Fujii, 2013]. This is a new mode of electromagnetic wave propagation in a terrestrial environment, which exhibits scientifically peculiar but interesting effects that have not been explained by conventional atmospheric and ionospheric theories.

Electromagnetic signals at the time of earthquakes have long been investigated in various frequency ranges from ultralow frequency (ULF) to very high frequency (VHF) [Fraser-Smith et al., 1990; Asada et al., 2001; Kushida and Kushida, 2002; Nagao et al., 2002; Fujiwara et al., 2004; Bakun et al., 2005; Hayakawa et al., 2007; Uyeda et al., 2009; Moriya et al., 2010]. The VLF electromagnetic signals show some records of possible fluctuation associated with earthquakes [Fraser-Smith et al., 1990; Asada et al., 2001], while another report claims no precursory signals even for a particularly targeted earthquake [Bakun et al., 2005]. High-frequency (HF) and VHF observations imply some possible association to earthquake precursors. There certainly are claims of both possibility and impossibility to the electromagnetic earthquake precursors. One might even conclude that prediction of earthquakes by monitoring such electromagnetic signals is not effective because earthquakes are random phenomena with respect to their potential precursors.

This paper is not an attempt to prove or disprove electromagnetic precursors of earthquakes but focuses on how the radio wave should act if mobile surface electrical charges exist on the ground, in particular, on mountain ranges. The phenomena would be scientifically interesting in that it is an interaction between the electromagnetic wave in the atmosphere and the surface plasmon on rough mountain surfaces, which, to the best of author's knowledge, has not yet been previously investigated.

The possibility of the generation of stress-induced electrical charges has been studied by laboratory experiments with various mechanisms suggested so far [Enomoto and Hashimoto, 1990; Freund, 2000, 2002, 2011;

Takeuchi and Nagao, 2013; Dahlgren et al., 2014], although it is beyond the scope of this paper to discuss in depth the charge generation mechanism associated with seismic activities. Freund et al. have experimentally shown that electrical particles of a positive charge come out of rocks when subjected to stresses [Freund, 2000, 2002, 2011; Bleier et al., 2013]. The electrical charge carriers are considered to be positive holes originating from the peroxy bonds broken by the stress. Dahlgren et al. have shown that the stress-stimulated current appears only from dry rocks, not from fluid-saturated rocks [Dahlgren et al., 2014]. Others have also suggested electrical carrier generation by seismic stresses, either positive or negative charges, with various mechanisms [Enomoto and Hashimoto, 1990; Takeuchi and Nagao, 2013]. It is rather plausible to consider that either of those mechanisms or similar ones may take place in reality. Note that the lifetime of the charged carriers is estimated from the experimental signals of the stress-induced current pulses to be over a wide range from the orders of milliseconds to hours, and even much longer [Scoville et al., 2015]. Those current pulses are observed intermittently or irregularly while stresses are applied in the experiments.

The electrical charges can thus be hypothetically considered to appear on the Earth's surface when tectonic stresses act somehow on underground rocks. If electrical charges exist on the surface of a conductor or possibly on an insulator as well due to some uncertain but possible mechanism, and if the charges are mobile, then the charges can oscillate collectively to carry energy. This is the surface plasma wave, or the surface plasmon, which is equivalent to the one in optics as light induces oscillation of electrons on flat metals and semiconductors [Kittel, 1986; Raether, 1977, 1988] or on metal spheres [Fujii, 2014]. It is shown in Fujii [2013] that similar oscillation of the surface charges can occur, which propagates along the ground surface, referred to in this paper as the terrestrial surface plasmon.

The surface plasmon can be intuitively understood by an analogy with a ripple wave that occurs on a water surface when a wind blows on a lake. Similarly, when an electromagnetic wave propagates over a conductive surface where electrical charges accumulate, the charges are forced to oscillate synchronously with the electromagnetic wave; moreover, when both the wavelength and the frequency of the electromagnetic wave match those of the eigenstate of the surface charge oscillation, a surface plasmon is strongly induced.

The author's previous paper [Fujii, 2013] shows the numerical evidence of the interaction between the terrestrial surface plasmon and the radio wave, mostly for the cases of topographically simple landforms, provided that surface charges exist on the ground. On the other hand, this paper considers more realistic geography that is modeled with a carefully measured three-dimensional digital elevation data of the actual landform, which include the rough and complicated surface of mountainous topography. Moreover, the digital geographic model is analyzed on a massively parallel super computer. The theory has also been extended to a more comprehensive form; various plasma frequencies of the surface electrical charges are considered with a recently measured charge density; thereby, it is clarified how the terrestrial surface plasmon is induced by the radio wave in the very high frequency (VHF) band. Note that the strength of the coupling between a surface plasmon and a radio wave depends on whether the plasma frequency is sufficiently higher than the radio wave frequency or not; if so, which can be the case of a strong seismic activity, the surface charges will interact strongly with the radio wave, and a surface plasmon will be excited strongly as well; if not, the case of no earthquake occurring, no surface plasmon will be excited by the radio wave either; if the plasma frequency is only slightly higher than the radio wave, which can be the case of a weak seismic activity, only a weak interaction will occur between them, and a surface plasmon will be excited weakly.

The mobile electrical charges diffuse by an electrical repulsive force during their lifetime and tend to reach transitionally to a state of lower energy on the Earth's surface; a part of them would move to a geographically sharp wedge or peak landform by the electrical repulsive force, i.e., possibly to a nearby peak of the mountain area. The terrestrial surface plasmon on a mountain peak certainly causes anomalous diffraction and scattering of the radio wave, thus causing the unusual long-distance propagation of radio waves even beyond mountains.

The paradoxical mechanism of the radio wave propagation beyond the line of sight is investigated in terms of the terrestrial surface plasmon associated with the stress-induced electrical charges of crustal rocks. This theory should contribute to the understanding of the causality between the underground seismic activity and the radio wave propagation in a broad area of a few hundred kilometers.

2. Theory of Terrestrial Surface Plasmon

This section describes the theoretical consideration of the surface plasmons on the Earth's surface, extended from the previous paper [Fujii, 2013] to the cases of various plasma frequencies. The frequency of the plasma oscillation, i.e., the plasma angular frequency ω_p or the plasma frequency f_p ,

$$\omega_p \equiv 2\pi f_p = \sqrt{\frac{nq^2}{\epsilon_0 m^*}} \quad (1)$$

is used to assess if the surface plasmon is induced on a conductive surface by an electromagnetic wave in free space; in equation (1), it is natural to choose the electrical charge q of the particle as that of an electron; i.e., $q = 1.60 \times 10^{-19}$ C of either positive or negative charge and $\epsilon_0 = 8.85 \times 10^{-12}$ F/m is the permittivity of vacuum. An uncertainty still exists, however, in choosing the number density of charged particles n and the effective mass of the particle m^* .

Recently, the number density of the charged particles n has been determined experimentally by applying a stress to a gabbro tile and measuring the outflowing electrical current [Scoville *et al.*, 2015]; the measured value of n has been found relatively constant, not very sensitive to how stresses are applied once exceeding a certain value, to be approximately 10^{15} to 10^{16} m⁻³. These values are considered particularly reasonable [Kamogawa and Ohtsuki, 1999] in terms of the comparison to other conductive and semiconductive materials; moreover, they produce reasonable effects of surface plasmons as shown in the later sections. On the other hand, the effective mass of the positive hole m^* is still uncertain. Considering the physical state of the positive hole, similar to the hole in the doped semiconductors, it is conceivable that it has a value several times larger than the static mass of an electron m_e , i.e., $m^* \approx m_e$ to $10 m_e$.

Now we consider the interface between the air and the ground, i.e., the permittivity of air $\epsilon_1 = \epsilon_0 \epsilon_{r1}$ with

$$\epsilon_{r1} = 1 \quad , \quad (2)$$

and the complex permittivity of the ground as a function of frequency $\epsilon_2 = \epsilon_0 \epsilon_{r2}$ with

$$\epsilon_{r2} = \epsilon'_{r2} - j\epsilon''_{r2} = \epsilon_\infty - j\frac{\sigma}{\epsilon_0 \omega} - \frac{\omega_p^2}{\omega^2 - j\omega\Gamma} \quad . \quad (3)$$

In equation (3), ϵ'_{r2} and ϵ''_{r2} denote the real and the imaginary parts of the complex permittivity ϵ_{r2} , respectively, j is the imaginary unit, ϵ_∞ is the relative permittivity of the ground at the limit of infinite frequency, σ is the conductivity of the ground, Γ is the damping factor, and ω the angular frequency of the radio wave [Fujii, 2013]. The second term in the right-hand side is the loss term. The third term is the Drude dispersion, which represents the response of the charged particles to the outer electric field, namely, the plasma oscillation [Kittel, 1986].

If the plasma frequency is higher than the frequency of the radio wave, the charged particle on the surface can follow the oscillation of the electrodynamic force by the radio wave, inducing a surface plasmon on the ground. Because the ground has a permittivity larger than that of air, the effective value of the plasma frequency on the ground can be defined by the frequency at which the permittivity transit from negative to positive values. In an ideal case where the loss terms of the permittivity in equation (3) are relatively small and negligible, i.e., $\sigma \ll 1$ and $\Gamma \ll \omega_p$, then letting $\epsilon_{r2} = 0$ in equation (3) gives the effective plasma frequency

$$f'_p = \frac{f_p}{\sqrt{\epsilon_\infty}} \quad , \quad (4)$$

which is plotted in Figure 1. In Figure 1, it is clear that for some ranges of n and m^* , f'_p is larger than the typical radio broadcast frequency, e.g., approximately from 70 MHz to 100 MHz. Three different values of $f'_p = 61, 163,$ and 408 MHz have been chosen to show later in the numerical analyses the behaviors of the surface plasmon propagation depending on f'_p .

In Figure 2, the complex permittivity (3) is plotted. The parameters chosen for it are the typical permittivity and conductivity of mixture of soils and rocks, i.e., $\epsilon_\infty = 6$ and $\sigma = 10^{-3}$ S/m, which are the same values as in Fujii [2013]. The plasma frequency is estimated from the appropriate ranges of n and m^* as $f_p = 1000, 400,$ and 150 MHz, i.e., $f'_p = 408, 163,$ and 61 MHz as shown in Figure 1, and $\Gamma = 2\pi \times 10^6$ rad/s by assuming that the damping factor of the charged particles is small enough compared to the plasma frequency.

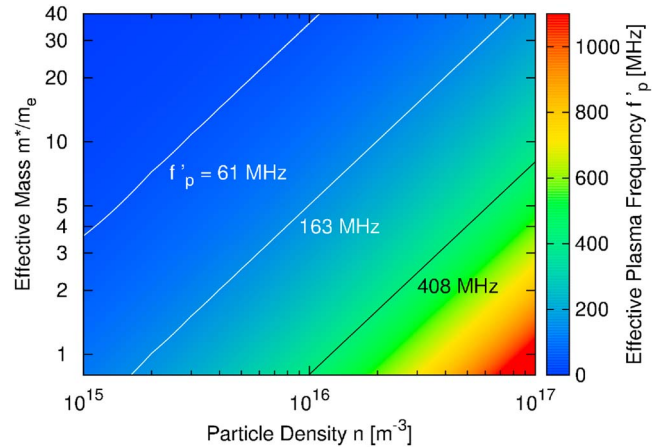


Figure 1. Color map of the effective plasma frequency f'_p as a function of particle density n and effective mass m^* . Three different values of $f'_p = 61, 163,$ and 408 MHz are indicated by solid contour lines, which are used in the later analyses.

The transitions from negative to positive values are clearly shown as the dip in the real part of the permittivity ϵ'_{r2} in Figure 2. The imaginary part of the permittivity ϵ''_{r2} is much smaller than ϵ'_{r2} at the radio broadcast frequency for $f'_p = 163$ and 408 MHz, but comparable with ϵ'_{r2} for $f'_p = 61$ MHz. The variations of the plasma frequency reflect the properties that, when the tectonic stress is at a high level, the charge carrier density at the surface n is high, leading to a higher plasma frequency; when the tectonic stress is low, so is n , thus lower plasma frequency.

Now we consider two different modes of waves on the interface between the air (with $\epsilon_{r1} = 1$) and the ground (with ϵ_{r2} of equation (3)); one is the nonplasmonic electromagnetic surface wave, i.e., the so-called Brewster mode [Collin, 1991] of the surface wave, and the other is the surface plasmon. For these modes of waves, it is possible to derive the analytical relation between the frequency and the wavelength, called the dispersion relation. It is expressed by the complex propagation constant γ , consisting of the attenuation constant α and the phase constant $\beta = 2\pi/\lambda$ with λ the wavelength, as

$$\gamma = \alpha + j\beta = j\frac{\omega}{c_0} \sqrt{\frac{\epsilon_{r1}\epsilon_{r2}}{\epsilon_{r1} + \epsilon_{r2}}}, \quad (5)$$

where c_0 is the velocity of light in vacuum [Raether, 1988].

The dispersion relation (5) of the surface plasmon is plotted in Figure 3 for the three values of the effective plasma frequency in Figure 1. It is clear that, for $f'_p = 408$ MHz and 163 MHz, the dispersion relation of the

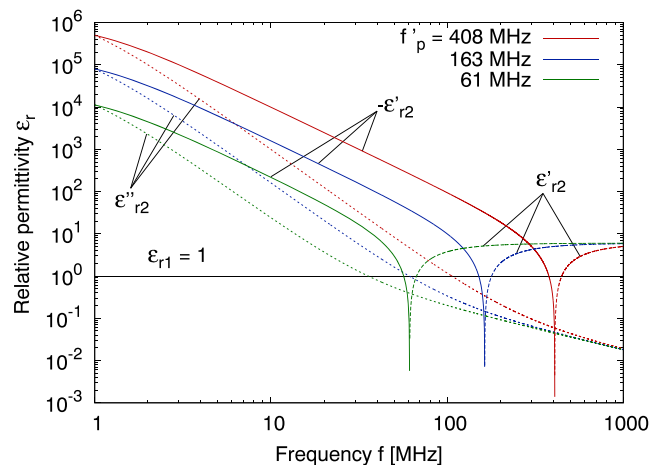


Figure 2. Complex permittivity (3) of the surface plasmons for the three different plasma frequencies f'_p .

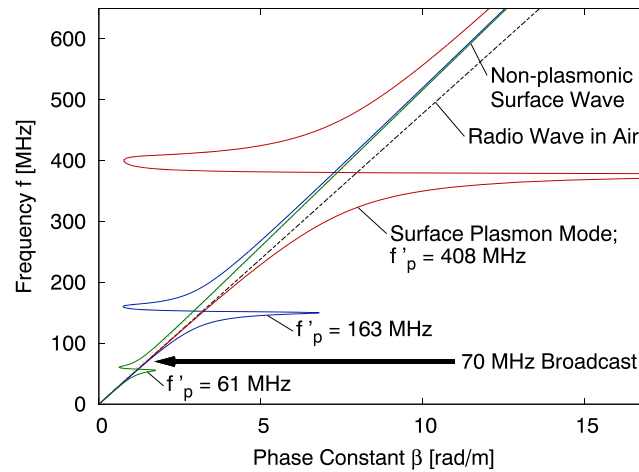


Figure 3. Dispersion relation of the surface plasmons for the three different plasma frequencies f'_p .

surface plasmon is close to the linear dispersion of the radio wave, i.e., the “light line” for the electromagnetic plane wave in the air, at the radio broadcast frequency 70 to 100 MHz. In these cases, the coupling between the surface plasmon and the radio wave becomes stronger, as the plasma frequency becomes higher, i.e., the dispersion curve of the surface plasmon approaches closer to the linear dispersion of the radio wave. In contrast, for $f'_p = 61$ MHz, which is lower than the radio broadcast frequency, e.g., at 70 MHz, the mode of propagation at 70 MHz is of the nonplasmonic surface wave, where no surface plasmon is induced by the radio wave. As a general consequence, it is noted that the higher the tectonic stress level, the higher the plasma frequency, and thus the stronger the surface plasmon induced, and vice versa.

3. Numerical Analysis

3.1. FDTD Analysis of Surface Plasmons

The finite-difference time-domain (FDTD) method [Yee, 1966; Taflov and Hagness, 2005] was used for the analysis in this study; it is a space-discrete method of solving Maxwell’s equations with the effect of surface charges taken into account by the form of an effective permittivity. The frequency-dependent complex permittivity (3), with either positive or negative real part, is transformed into a time-dependent differential equation and solved together with Maxwell’s equations.

The accuracy of the method has been verified extensively in various problems [Taflov and Hagness, 2005], e.g., optical solitons [Fujii et al., 2005] and nanooptics [Fujii et al., 2008; Fujii, 2010, 2012, 2014, and references therein]. The same method has been applied to the analysis of the surface plasmon on planar and curved

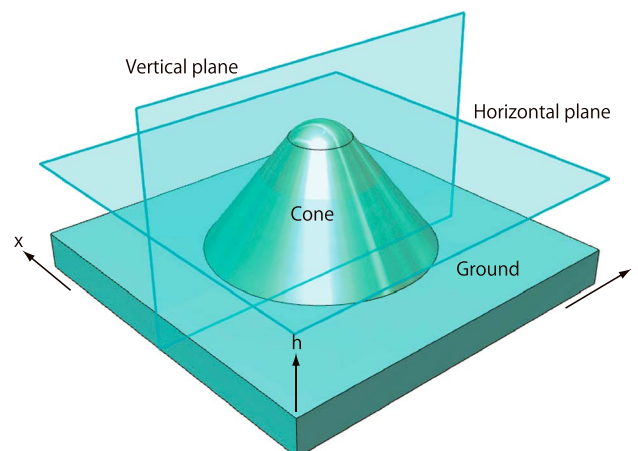


Figure 4. Analysis configuration of the round-tip cone on the ground.

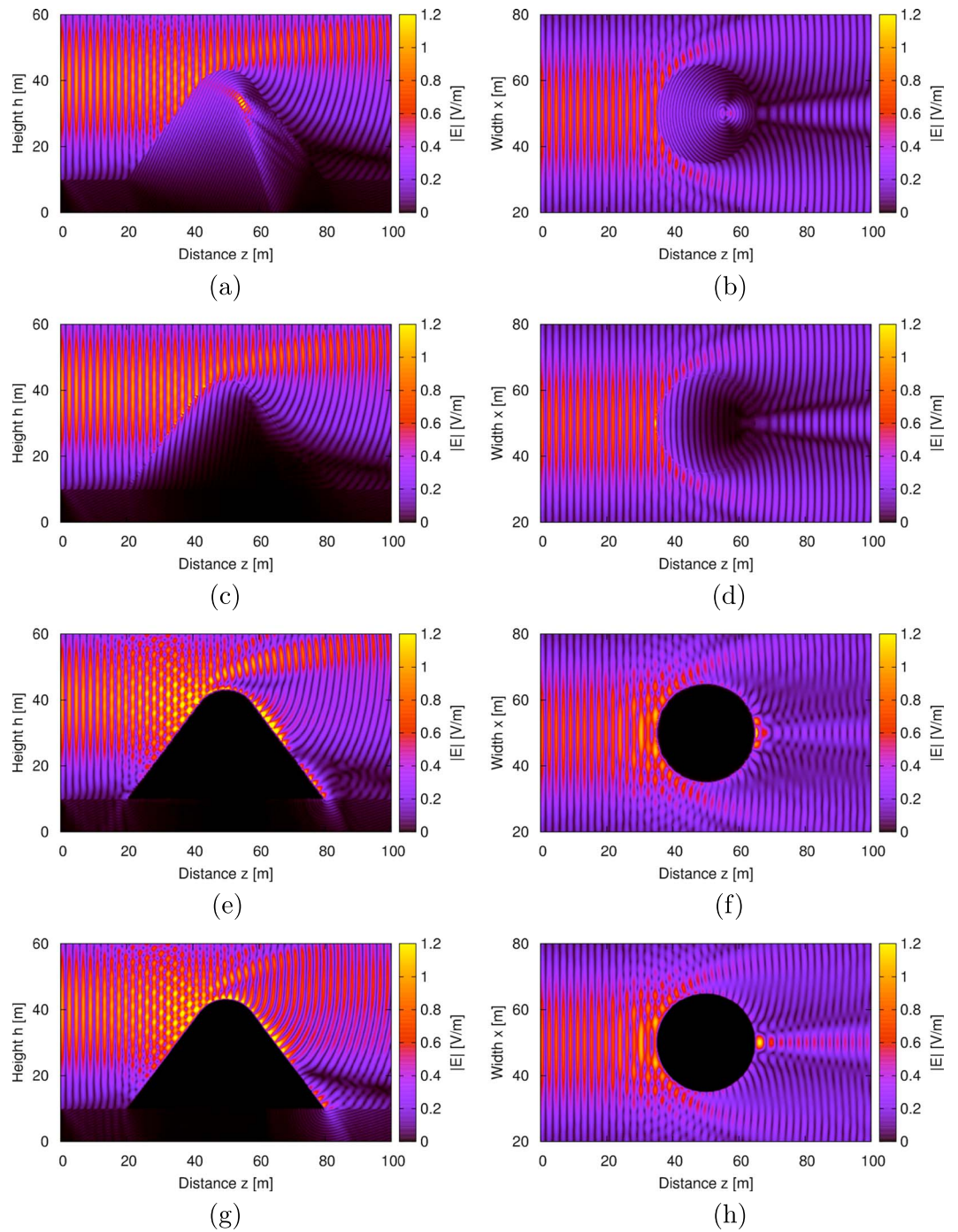
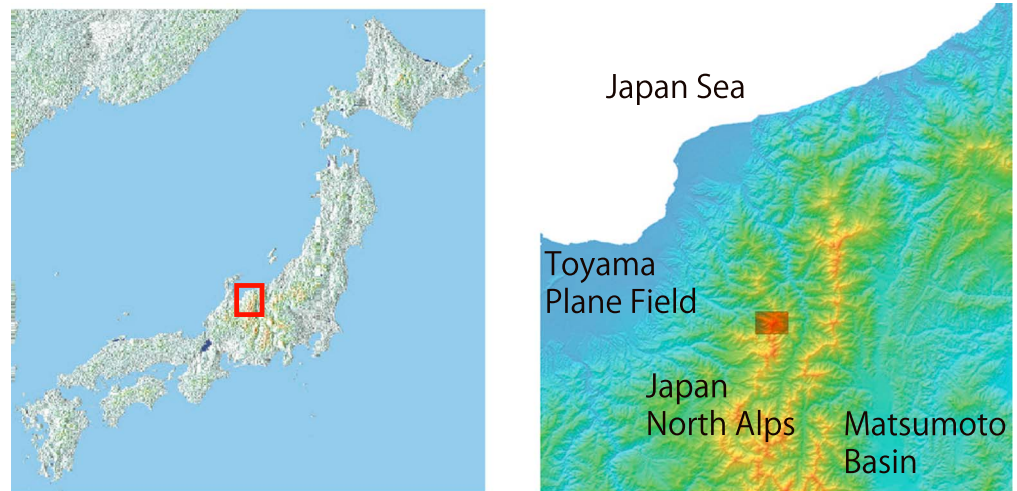


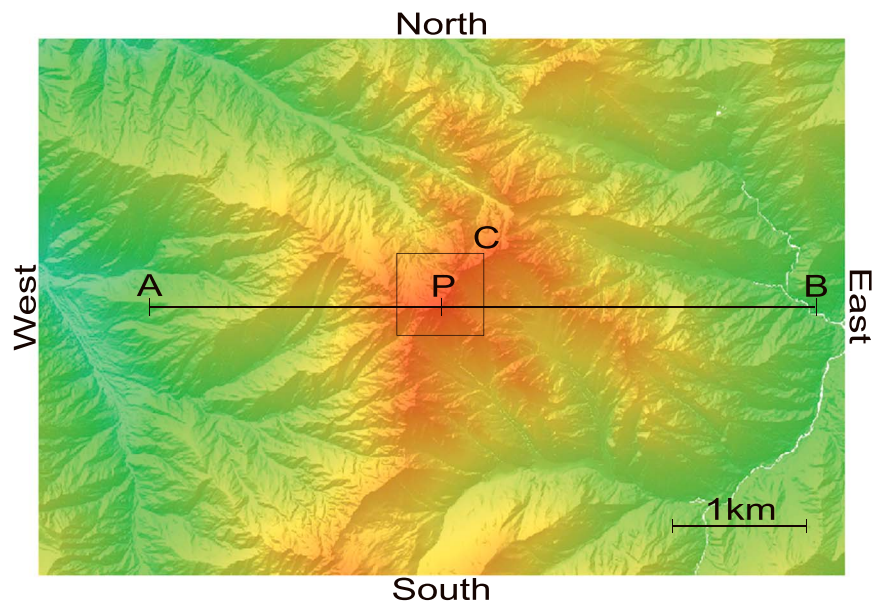
Figure 5. Scattering of an electromagnetic wave by the conical structure with and without the surface charges of various plasma frequencies. Absolute value of the electric field $|E|$ is shown. (a, b) Without surface charges, (c, d) with surface charges of $f'_p = 61$ MHz, (e, f) with surface charges of $f'_p = 163$ MHz, and (g, h) with surface charges of $f'_p = 408$ MHz; Figures 5a, 5c, 5d, and 5g are plotted on the vertical plane, and Figures 5b, 5d, 5f, and 5h are on the horizontal plane.

geometries [Fuji, 2013]. The results have been found consistent with the reported observations [Kushida and Kushida, 2002; Moriya et al., 2010]. In principle, linear Maxwell's equations are invariant if the time and the space sizes are scaled with the wavelength; the numerical accuracy is retained also for the analysis of the terrestrial surface plasmons.



(a)

(b)



South

(c)



(d)

Figure 6. Geological location and view of the analysis region. (a) Map of Japan, the red rectangle is the mountainous north Japan Alps area of Japan main island. (b) Expansion of the red rectangle of Figure 6a, i.e., the north Japan Alps district considered in this work. The red rectangle patch is the region for the numerical analysis. (c) Digital elevation model of the Tsurugidake peak, for the region of the red patch in Figure 6b, i.e., area of 6 km in west to east (horizontal axis) and 4 km in south to north (vertical axis) and the peak point P. (d) The view of the Mount Tsurugidake peak from the west. The image is approximately 3000 m horizontally and 800 m vertically from 2200 m to 3000 m in altitude. The view point is slightly rotated from the west to the north. Figures 6a–6c are from the Geographical Survey Institute, Japan, Figure 6d is by the author.

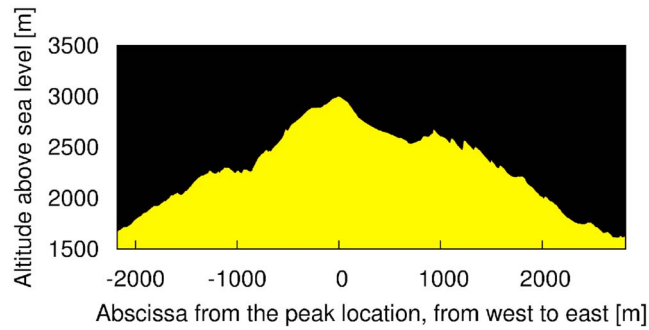


Figure 7. Configuration of the relative dielectric constant for the whole 2-D analysis model, spanning 5 km distance from west to east, and 2 km vertical. The black region is air with $\epsilon_{r1} = 1$, and the yellow region represents the mountain body with $\epsilon_{\infty} = 6$.

The geographical scale of mountains is, on the other hand, much larger than the wavelength of the radio wave, and thus the FDTD analysis will be a large-scale numerical problem. For the analyses in this paper, a massively parallel supercomputer GB8000 at Kyoto University, Japan, was used, where maximum 64 nodes, 1024 processors, and 3.8 TB memory were available.

3.2. Preliminary Analysis of Cone-Like Structure

For verification, the surface plasmon is first analyzed on an ideal cone structure shown in Figure 4; the conical point has been rounded in order to avoid the field singularity on the sharp tip, which often causes numerical errors. The size of the analysis region is width 100 m in x , length 100 m in z , and height 43.333 m in y directions.

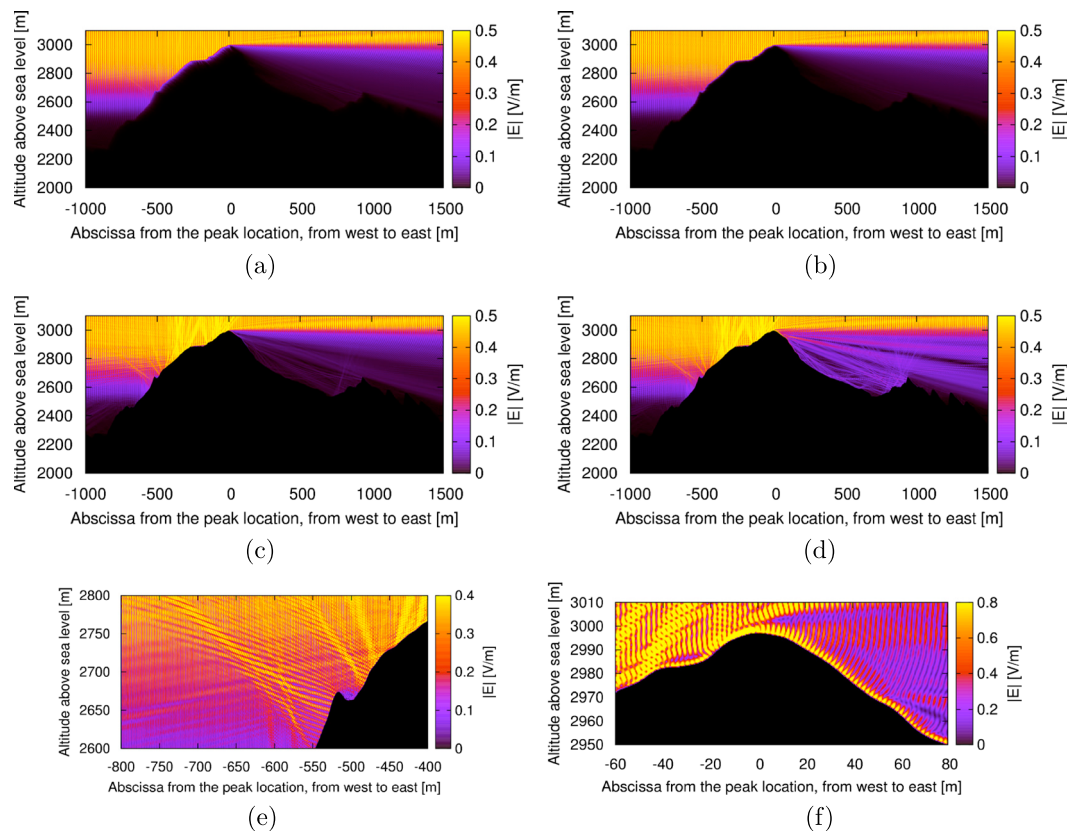


Figure 8. Results of the 2-D analysis for the incident wave from the west of the peak. Absolute value of the electric field $|E|$ is plotted on the plane of Figure 7. (a) Without surface charges, (b) with surface charges of $f_p' = 61$ MHz, (c) with surface charges of $f_p' = 163$ MHz, and (d) with surface charges of $f_p' = 408$ MHz. (e) Expansion of Figure 8d for the west part of the peak and (f) expansion of Figure 8d at the peak point.

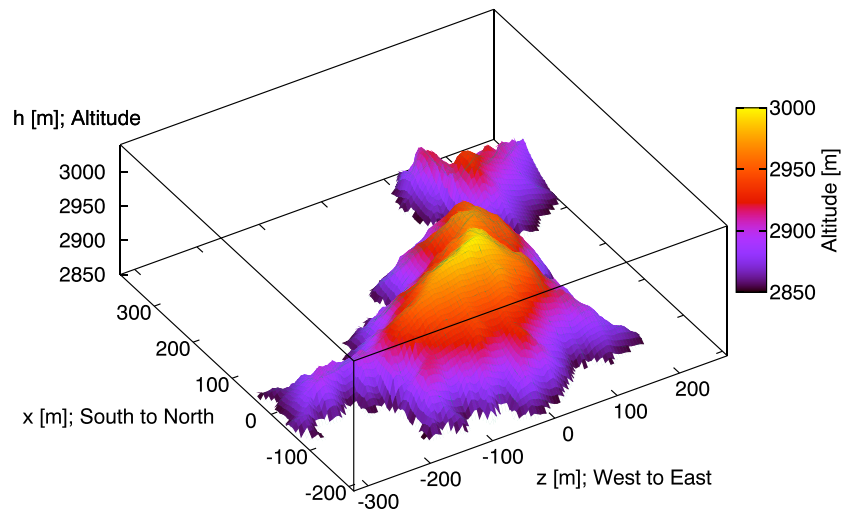


Figure 9. The 3-D analysis configuration of the Tsurugidake peak. The thin grid shows the original digital elevation model of approximately 5 m resolution. The origin of the horizontal axes is collocated with the peak. Altitude h is taken in the y direction.

The cone is placed on the ground of thickness 10 m, the radius of its base circle is 30 m; the original cone was 40 m high from the base to the tip, and the tip was rounded off to a spherical curve of 10 m in radius.

The electrical property of the ground is a dielectric of relative permittivity $\epsilon_{\infty} = 6$ and conductivity $\sigma = 10^{-3}$ S/m, and that of the cone was chosen to be (i) a uniform dielectric of $\epsilon_{\infty} = 6$ and $\sigma = 10^{-3}$ S/m without surface charges, (ii) a dielectric of $\epsilon_{\infty} = 6$ and $\sigma = 10^{-3}$ S/m with surface charges of the effective plasma frequency $f'_p = 61$ MHz, (iii) similar to case (ii) but with $f'_p = 163$ MHz, and (iv) similar to case (ii) but with $f'_p = 408$ MHz.

An electromagnetic wave was launched at frequency 70 MHz from $z = 0$ with nearly a plane wave form of the maximum electric field 1 V/m to illuminate the upper part of the cone. The whole structure was modeled with a discretization of 0.2 m cubic Yee cell. The computation was performed with 128 processors and 300 GB memory on GB8000. The calculation time was less than 2 h each.

The results are shown in Figure 5. The electric field strength is plotted on the vertical and the horizontal planes of Figure 4. For the case without surface charges (i), the cone is a simple dielectric, and the wave penetrates into it as shown in Figures 5a and 5b. For the dielectric with surface charges and $f'_p = 61$ MHz (ii), since the effective plasma frequency is lower than the radiated wave, the cone behaves practically as a dielectric, and as in Figures 5c and 5d the wave also penetrates into the cone as a nonplasmonic surface wave. For the cases of more surface charges, i.e., higher plasma frequency of the cases (iii) and (iv), the incident wave is reflected at the surface of the cone as shown in Figures 5e, 5f, 5g, and 5h; interestingly, the surface plasmon is induced and propagates along the round tip of the cone, even downward reaching to the ground. Furthermore, the surface plasmon radiates an electromagnetic wave in the form of a remarkably narrow beam into the air toward the limited direction just opposite from the incident wave; see Figures 5f and 5h. The secondary wave radiated from the surface plasmon is stronger for the case of higher plasma frequency (iv) in Figures 5g and 5h, than for case (iii) in Figures 5e and 5f.

3.3. Analysis of the Peak of the Japan Alps

Japan has a mountainous land structure of Figure 6a, particularly in the middle part comprising north, central, and south mountain ranges called, as a whole, the Japan Alps. They are chains of approximately 3000 m peaks. On each side of the Japan Alps, there are plane fields and basins with urban districts as shown in Figure 6b; the mountain range in this district is the north Japan Alps. In this paper, one of those peaks called Tsurugidake of Figure 6c is analyzed. A digital elevation model (DEM) of the landform has been developed on a grid as fine as 5 m resolution for the most part of Japan, provided freely by the Geographical Survey Institute, Japan.

The reasons to choose the Tsurugidake peak are as follows. (i) A complete digital elevation model is available for this peak. (ii) It is close to a city, approximately 40 km from the city center of Toyama, thus the influence to

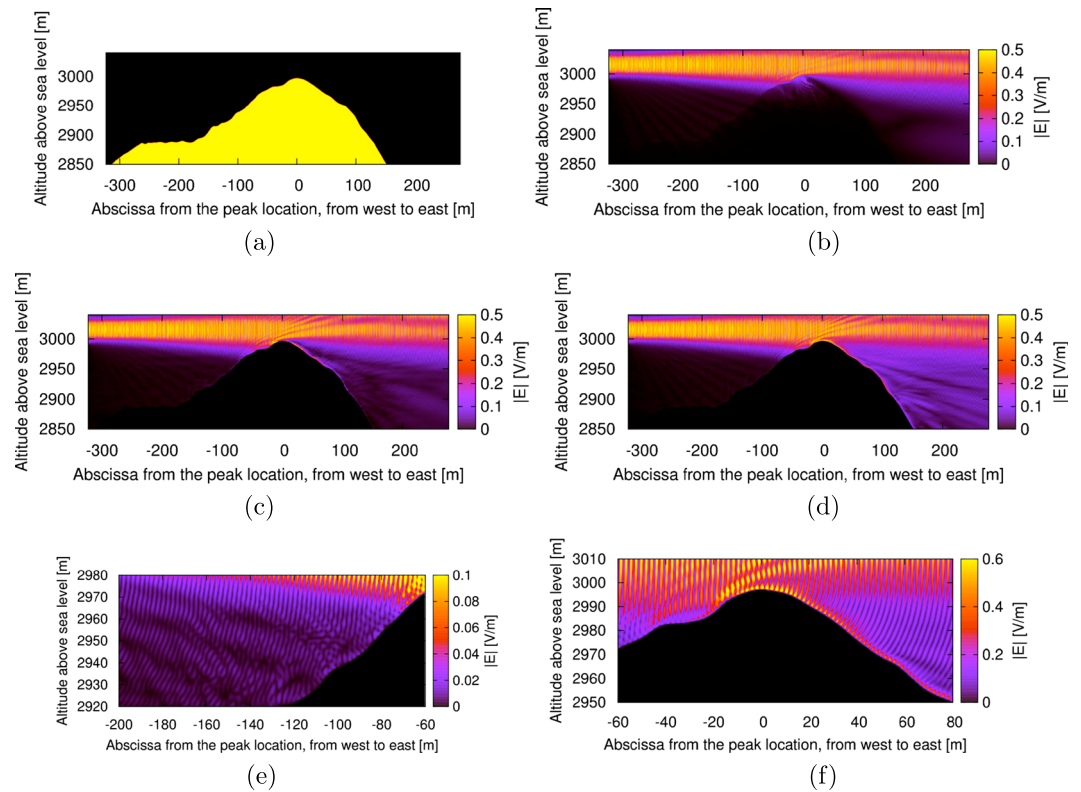


Figure 10. Results of the 3-D analysis for the incident wave from the west of the peak. Absolute value of the electric field $|E|$ is plotted on the vertical plane of $x = 0$. (a) Configuration of the relative dielectric constant for the 3-D model on the plane of $x = 0$; the black region is air with $\epsilon_{r1} = 1$, and the yellow region represents the mountain body with $\epsilon_{\infty} = 6$. (b) Field without surface charges, (c) with surface charges of $f'_p = 163$ MHz, and (d) with surface charges of $f'_p = 408$ MHz. (e) Expansion of Figure 10d for the west part of the peak and (f) expansion of Figure 10d at the peak point.

the radio wave is considered strong. (iii) The peak is 2999 m in altitude, one of the highest peaks in this district. (iv) The tree line is at approximately 2500 m in this district, and Tsurugidake has a rocky steep peak without trees as seen in Figure 6d; hence, the dielectric property can be modeled accurately by that of typical rocks, without considering the effects of other objects like trees.

The numerical model was derived for the Tsurugidake peak separately in the two-dimensional (2-D) space and in the three-dimensional (3-D) space. The 2-D model is along the line segment AB of 5 km distance in Figure 6c, and the 3-D model is on the square C of 600 m \times 600 m area in the same figure; the center P of Figure 6c is the peak. The 2-D model is analyzed for a longer distance and larger altitude range than the 3-D model; the 3-D model is however analyzed for a more realistic roughness in its surface topography.

The mountain body is modeled with the dielectric constant $\epsilon_{\infty} = 6$ and electric conductivity $\sigma = 10^{-3}$ S/m, with or without the plasma property of effective plasma frequency $f'_p = 408$ MHz, which has been estimated from the number density of the positive hole $n \approx 10^{15}$ to 10^{16} m $^{-3}$ by the theory in the previous section. If the radio wave frequency is lower than the effective plasma frequency f'_p , the surface plasmon is induced by the radio wave, but if not, no plasmon is induced. The radio wave is excited from the west of the peak with the maximum electric field 1 V/m polarized in the vertical y direction for both the 2-D and the 3-D analyses.

To ensure the numerical accuracy, the grid resolution should be finer than 1/20 of the wavelength. In this paper, the radio wave is chosen for all the analyses to be in the very high frequency (VHF) band at frequency 70 MHz, of which wavelength is 4.3 m. On the other hand, the digital elevation model by the Geographical Survey Institute is approximately 5 m resolution, comparable to the wavelength; hence, it is necessary to regenerate a finer grid for the FDTD analysis. To do this, the bicubic spline interpolation was used [Press et al., 1992], successfully deriving a smooth grid of 0.2 m resolution from the 5 m resolved grid.

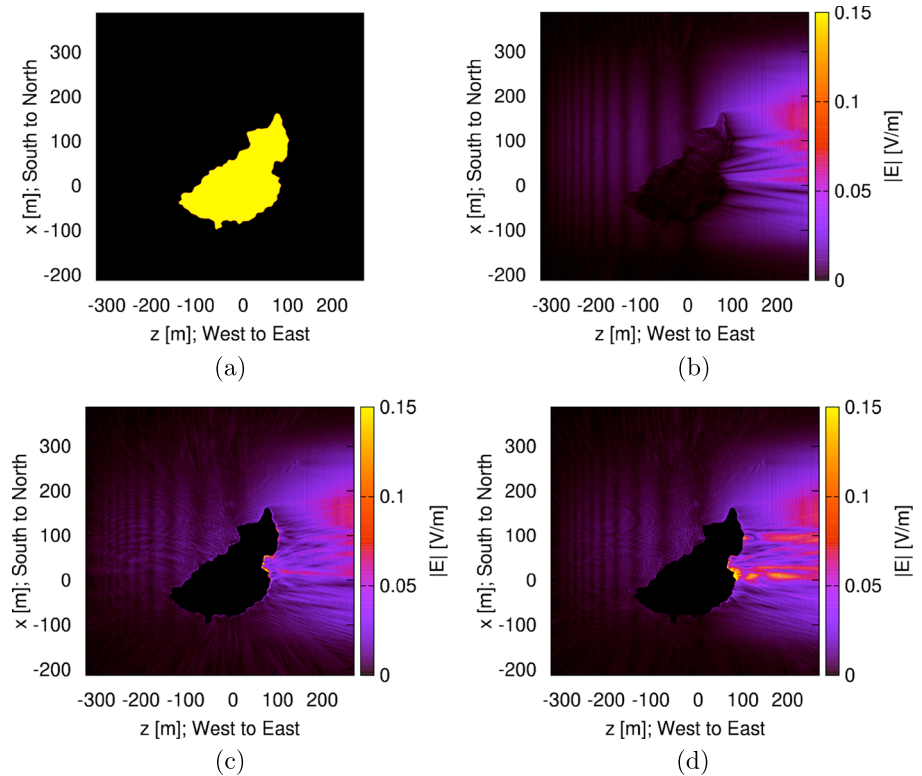


Figure 11. Results of the 3-D analysis for the incident wave from the west of the peak. Absolute value of the electric field $|E|$ is plotted on the horizontal plane at altitude 2940 m. (a) Configuration of the relative dielectric constant for the 3-D model on the plane at altitude 2940 m; the black region is air with $\epsilon_{r1} = 1$, and the yellow region represents the mountain body with $\epsilon_{\infty} = 6$. (b) Field without surface charges, (c) with surface charges of $f_p' = 163$ MHz, and (d) with surface charges of $f_p' = 408$ MHz.

3.3.1. Two-Dimensional Analysis

The geological configuration of Figure 7 is analyzed for the 2-D model, i.e., considering the variation only in the y direction of height and the z direction of distance from west to east, respectively. The incident wave is launched from the west with the maximum electric field of 1 V/m and polarized in the y direction, so that the incident wave closely touches the peak in order to see how the surface plasmon interacts with the radio wave at the peak. The necessary computational resource was 550 processors, 570 GB memory on GB8000, and each analysis took 12 h.

The results are shown in Figure 8. For the case where no surface charge exists as in Figure 8a, the electromagnetic wave is partly intercepted by the peak, and the upper part of it propagates over the peak to the east; besides, a particularly weak diffraction is imperceptibly seen, propagating slightly downward. For the case where the surface charges exist and the effective plasma frequency is 61 MHz, i.e., lower than the radio wave of 70 MHz as in Figure 8b, the result is similar to Figure 8a, because no surface plasmon is induced. In contrast to these two cases, when the effective plasma frequency is 163 MHz and 408 MHz, i.e., higher than the radio wave for Figures 8c and 8d, respectively, it is interesting to note that strong waves are radiated downward from the peak to the east. Scattered waves also propagate in various directions both upward and downward as shown in the expanded figure of Figure 8e. The surface plasmon induced at the peak is clearly seen in the expanded figure of Figure 8f, which propagates downward along the surface of the mountain, with radiating electromagnetic wave also downward.

3.3.2. Three-Dimensional Analysis

The analysis configuration of the 3-D model is shown in Figure 9. Unlike the 2-D analysis, the 3-D analysis considers all the physical dimensions, thus clarifying the influence of the actual rough mountain surface to the surface plasmon. The disadvantage of the 3-D analysis is to require large computational resources. For the 3-D analysis, the maximum 1024 processors and 3.8 TB memory were used on GB8000 to analyze a

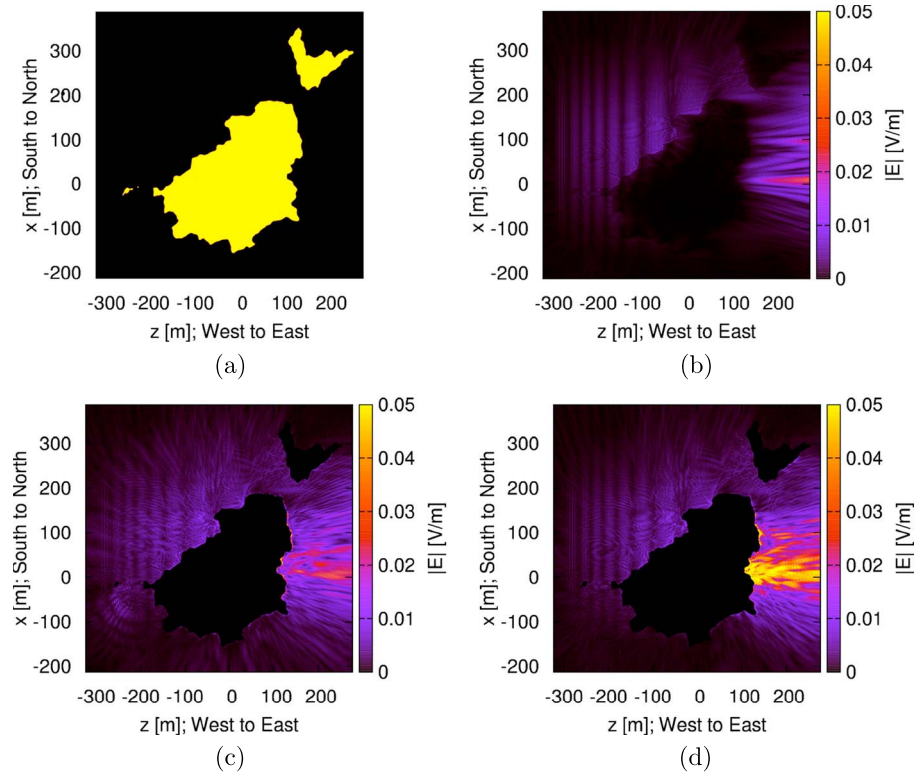


Figure 12. Results of the 3-D analysis for the incident wave from the west of the peak. Absolute value of the electric field $|E|$ is plotted on the horizontal plane at altitude 2900 m. (a) Configuration of the relative dielectric constant for the 3-D model on the plane at altitude 2900 m; the black region is air with $\epsilon_{r1} = 1$, and the yellow region represents the mountain body with $\epsilon_{\infty} = 6$. (b) Field without surface charges, (c) with surface charges of $f'_p = 163$ MHz, and (d) with surface charges of $f'_p = 408$ MHz.

600 m \times 600 m \times 190 m space including the peak with 0.2 m FDTD grid resolution. The calculation time was approximately 6 h each.

The radio wave is first excited from the west of the peak with 1 V/m maximum electric field polarized in the y direction, in the similar manner as in the 2-D analysis. The results are shown in Figure 10; the surface plasmon induced on the mountain peak has been found similar to that in the 2-D analysis. Figure 10a is the configuration of the relative dielectric constant on the plane of cross section at $x = 0$, and the field is plotted on the same plane. Without surface charges, as shown in Figure 10b, although the radio wave hits the peak, only a weak diffraction is observed. Since the model is 3-D, the incident wave can also go around the mountain-side and circumvent the peak. In contrast, for the cases where surface charges exist and $f'_p = 163$ MHz and 408 MHz as in Figures 10c and 10d, respectively, a strong field of the surface plasmon is observed along the curve of the peak, which reradiates electromagnetic waves downward into the air; as expected, Figure 10d shows more intense radiated fields than those in Figure 10c.

The detail of the electric field is plotted in Figures 10e and 10f. The reflected wave in Figure 10e is found weaker than the case of 2-D; however, the figure shows a fluctuating interference pattern together with the incident wave, which implies the existence of the reflected wave. At the peak point, the surface plasmon is clearly induced and propagates along the surface of the mountain as in Figure 10f. These results correspond well with those of the 2-D analyses. In general, the wave field analyzed in the 3-D space is slightly weaker than that in 2-D, which is a reasonable consequence because the field spreads in all directions in 3-D, whereas for 2-D, the spreading direction is limited and the wave is rather confined. Accordingly, the results for the 2-D and the 3-D cases are consistent; thereby, the analysis results are considered reliable.

In Figures 11 and 12, the electric fields are plotted on the horizontal plane of the cross section at altitudes 2940 m and 2900 m, respectively. In Figures 11a and 12a, the configuration of the relative dielectric constant is shown. The difference of the field strength in Figures 11b–11d and 12b–12d shows that the higher the

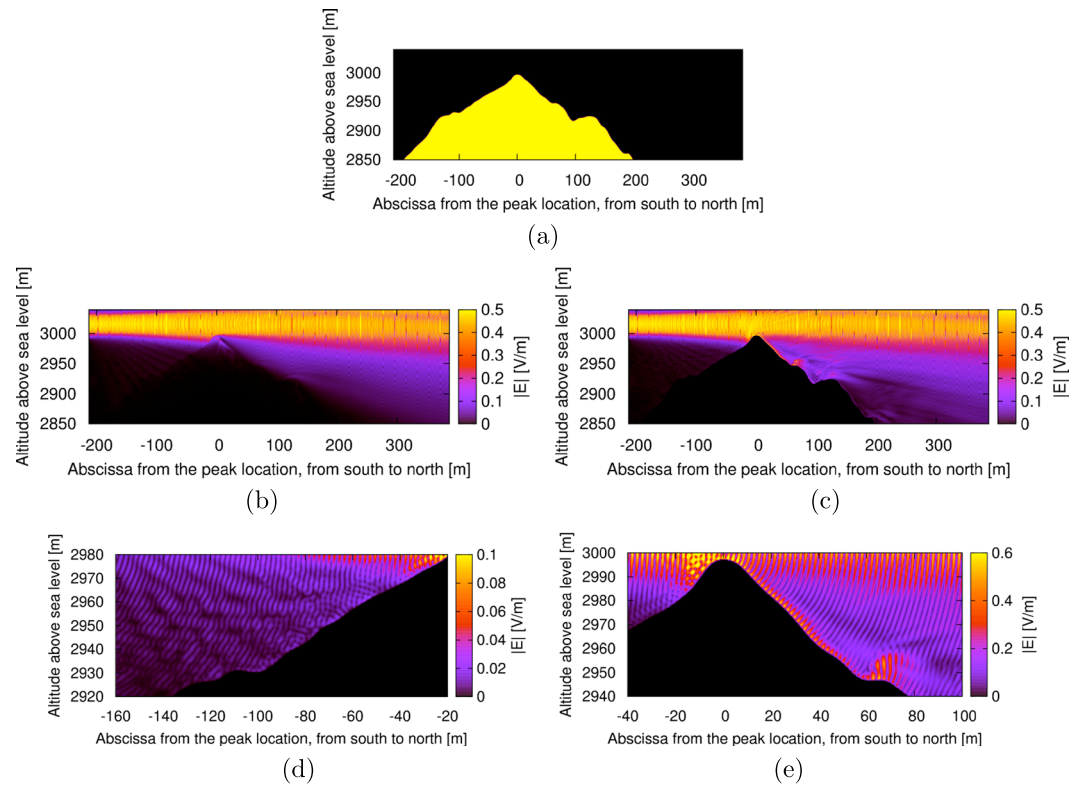


Figure 13. Results of the 3-D analysis for the incident wave from the south of the peak. Absolute value of the electric field $|E|$ is plotted on the vertical plane of $z = 0$. (a) Configuration of the relative dielectric constant for the 3-D model on the plane of $z = 0$; the black region is air with $\epsilon_{r1} = 1$, and the yellow region represents the mountain body with $\epsilon_{\infty} = 6$. (b) Field without surface charges, and (c) with surface charges of $f_p' = 408$ MHz. (d) Expansion of Figure 13c for the south part of the peak, and (e) expansion of Figure 13c at the peak point.

plasma frequency is, the stronger the surface plasmon is induced, and thus the stronger the electromagnetic wave reradiated into the air. In addition, the roughness of the mountain surface randomly scatters the surface plasmon, but the radiated wave is rather narrowly convergent beam-like wave, limited in its propagation directions. This is a surprising but interesting feature; i.e.m the fields radiated from the surface plasmon can be received only at limited places.

The surface of the mountain is significantly rough with respect to the radio wavelength, which causes a random propagation of the surface plasmon and the diffracted fields. To show the universality of the random interaction, we analyzed the same peak configuration with different incident directions. In Figure 13, the radio wave incident from the south of the peak is also analyzed as an example. The peak configuration on the cross section perpendicular to the z axis is shown in Figure 13a. Figures 13b and 13c are the comparison between the cases with and without surface charges. For this incident direction, although the peak curvature is sharper than in the previous analysis in Figure 10a, the surface plasmon propagates in the similar manner along the mountain surface. Interestingly, it has a bump halfway down on the northern side; without surface charges as in Figure 13b, the field exhibits practically no effect, while with surface charges, the surface plasmon in Figure 13c shows strong scattering from the bump. A weak reflected wave is also slightly visible in Figure 13d as a fluctuated interference pattern. The propagation of the surface plasmon and the reradiation of the wave is clearly seen in the expanded figure Figure 13e.

The surface plasmon is more enhanced for the incident wave from the south than that from the west. The radiated field is much stronger with the surface charges in Figures 14c and 15c than those cases without surface charges in Figures 14b and 15b. It is observed that the rough surface of the mountain strongly scatters the surface plasmon. The radiated electromagnetic wave is also narrowed into more intense beams as in the previous case of Figures 11 and 12.

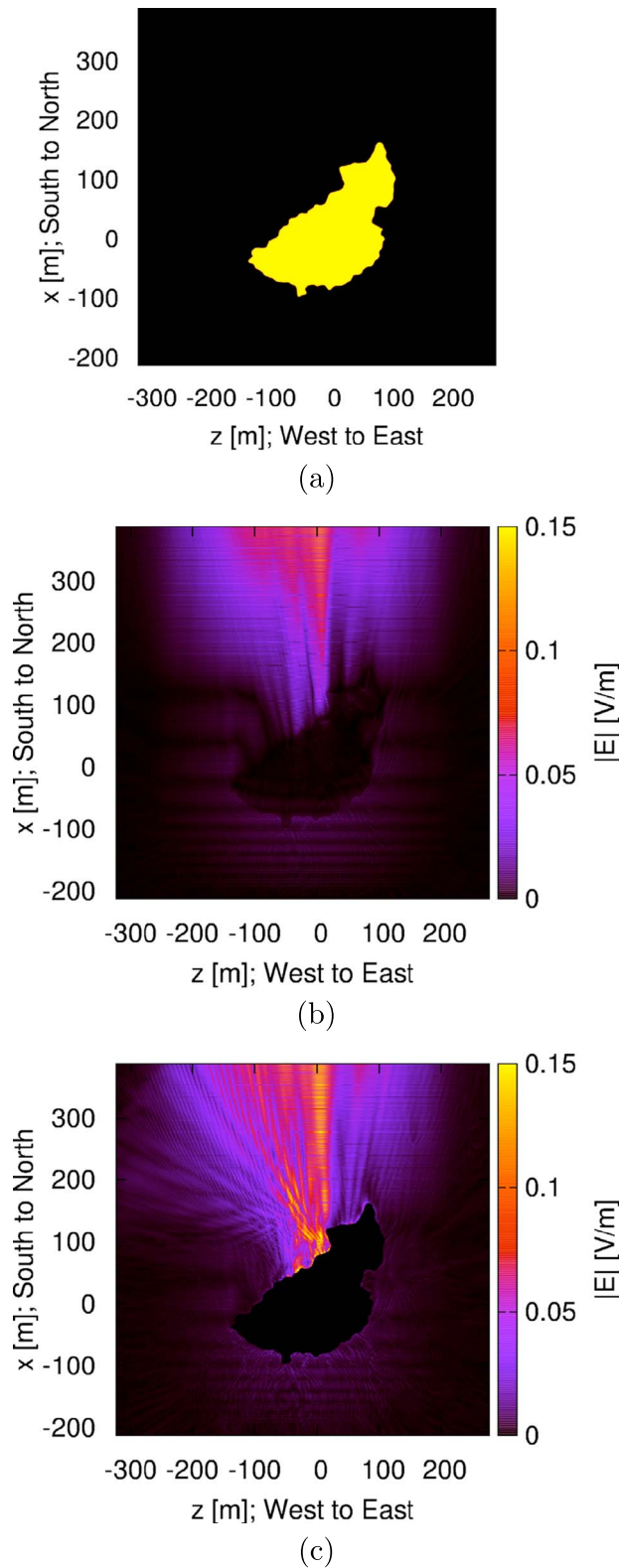


Figure 14. Results of the 3-D analysis for the incident wave from the south of the peak. Absolute value of the electric field $|E|$ is plotted on the horizontal plane at altitude 2940 m. (a) Configuration of the relative dielectric constant for the 3-D model on the plane at altitude 2940 m; the black region is air with $\epsilon_{r1} = 1$, and the yellow region represents the mountain body with $\epsilon_{\infty} = 6$. Same as Figure 11a. (b) Field without surface charges and (c) with surface charges of $f'_p = 408$ MHz.

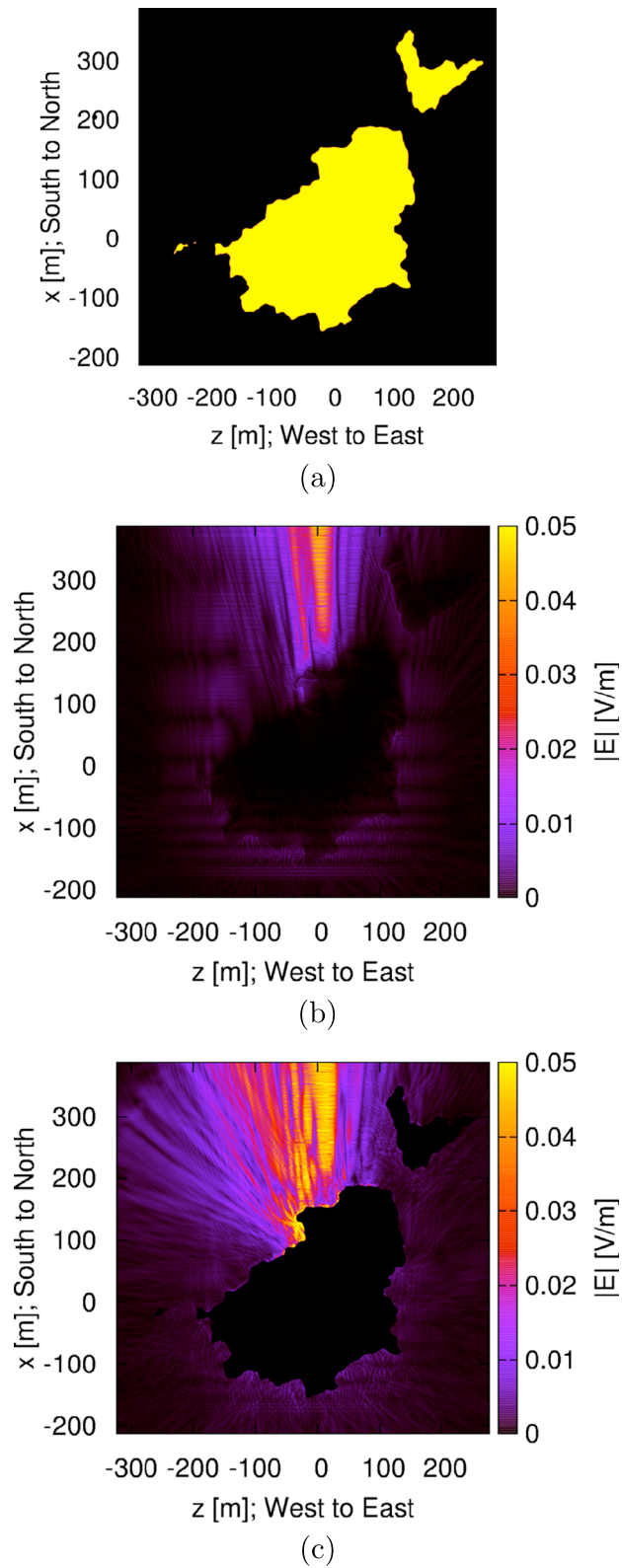


Figure 15. Results of the 3-D analysis for the incident wave from the south of the peak. Absolute value of the electric field $|E|$ is plotted on the horizontal plane at altitude 2900 m. (a) Configuration of the relative dielectric constant for the 3-D model on the plane at altitude 2900 m; the black region is air with $\epsilon_{r1} = 1$, and the yellow region represents the mountain body with $\epsilon_{\infty} = 6$. Same as Figure 12a. (b) Field without surface charges and (c) with surface charges, $f'_p = 408$ MHz.

4. Discussions and Conclusions

From the numerical results presented in this work, it is considered possible that radio waves propagate along mountain surfaces beyond the line of sight and are scattered and diffracted randomly from a mountain peak if electrical charges exist on the peak by a certain seismic forces acting on the crustal rocks. This is occasionally possible if the electrical charges diffuse by electrical repulsive forces in their lifetime of the orders of milliseconds to hours and even longer, and some of them move from a fault zone to a physically sharp landform like mountain peaks. The charges then act as terrestrial surface plasmons and interact with radio waves as a secondary source of the radio waves.

The most important finding is that the radio wave is reradiated randomly in the form of a narrowly convergent wave; thus, the reradiated wave can be received only at limited locations. Such a radio wave anomaly depends on the amount of electrical charges, namely, the strength of the terrestrial surface plasmon. This randomness nature suggests that the radio wave anomaly may or may not be detected at an identical locations depending on the stress to the rocks.

By continually observing the radio wave anomaly, the seismic activity can be monitored over a relatively broad region within a few hundred kilometers from a broadcast station. In contrast, the direct detection of the electrical phenomena, such as the electrical current and the field intensity, which should be measured locally, may not be sufficiently stronger than the other electromagnetic noises. Radio wave observatories built at various locations each with a few hundred kilometers apart would enable to predict the area where the seismic activity is strong. Probably the most effective way is to combine the conventional long-term prediction based on the historical records of seismology with the local detection techniques of physical quantities such as the electrical currents and fields, together with monitoring the radio wave anomalies over broader areas.

Acknowledgments

This work is partly supported by the Japan Society for the Promotion of Science (JSPS) KAKENHI grant 15K13971 and by the large-scale computing collaborative program of the Institute for Information Management and Communication, Kyoto University, Japan. The numerical data in this manuscript can be obtained from the author Masafumi Fujii, mfujii@eng.u-toyama.ac.jp.

References

- Asada, T., H. Baba, M. Kawazoe, and M. Sugiura (2001), An attempt to delineate very low frequency electromagnetic signals associated with earthquakes, *Earth Planets Space*, *53*, 55–62.
- Bakun, W. H., et al. (2005), Implications for prediction and hazard assessment from the 2004 Parkfield earthquake, *Nature*, *437*(13), 969–974.
- Bleier, T., et al. (2013), *Earthquake Prediction Studies: Seismo Electromagnetics*, edited by M. Hayakawa, pp. 113–128, Terrapub, Tokyo.
- Collin, R. E. (1991), *Field Theory of Guided Waves*, 2 ed., pp. 697–704, IEEE Press, New York.
- Dahlgren, R., M. Johnston, V. Vanderbilt, and R. Nakaba (2014), Comparison of the stress-stimulated current of dry and fluid-saturated gabbro samples, *Bull. Seismol. Soc. Am.*, *104*(6), 2662–2672.
- Enomoto, Y., and H. Hashimoto (1990), Emission of charged particles from indentation fracture of rocks, *Nature*, *346*, 641–643.
- Fraser-Smith, A. C., A. Bernardi, P. R. McGill, M. E. Ladd, R. A. Helliwell, and J. O. G. Villard (1990), Low-frequency magnetic field measurements near the epicenter of the M_s 7.1 Loma Prieta earthquake, *Geophys. Res. Lett.*, *17*(9), 1465–1468.
- Freund, F. (2000), Time-resolved study of charge generation and propagation in igneous rocks, *J. Geophys. Res.*, *105*(B5), 11,001–11,019.
- Freund, F. (2002), Charge generation and propagation in igneous rocks, *J. Geodyn.*, *33*, 543–570.
- Freund, F. (2011), Pre-earthquake signals: Underlying physical processes, *J. Asian Earth Sci.*, *41*, 383–400.
- Fujii, M. (2010), Finite-difference analysis of plasmon-induced forces of metal nano-clusters by the Lorentz force formulation, *Opt. Exp.*, *18*(26), 27,731–27,747.
- Fujii, M. (2012), Correction and verification of dispersion and loss of plasmons on metal nano-spheres, *J. Lightwave Technol.*, *30*(9), 1284–1290.
- Fujii, M. (2013), Theory of ground surface plasma wave associated with pre-earthquake electrical charges, *Radio Sci.*, *48*, 122–130.
- Fujii, M. (2014), Fundamental correction of Mie's scattering theory for the analysis of plasmonic resonance of a metal nanosphere, *Phys. Rev. A: At. Mol. Opt. Phys.*, *89*(3), 033805.
- Fujii, M., N. Omaki, M. Tahara, I. Sakagami, C. Poulton, W. Freude, and P. Russer (2005), Optimization of nonlinear dispersive APML ABC for the FDTD analysis of optical solitons, *IEEE J. Quantum Electron.*, *41*(3), 448–454.
- Fujii, M., W. Freude, and J. Leuthold (2008), Numerical prediction of minimum sub-diffraction-limit image generated by silver surface plasmon lenses, *Opt. Exp.*, *16*(25), 21039.
- Fujiwara, H., et al. (2004), Atmospheric anomalies observed during earthquake occurrences, *Geophys. Res. Lett.*, *31*, L17110.
- Hayakawa, M., V. V. Surkov, Y. Fukumoto, and N. Yonaiguchi (2007), Characteristics of VHF over-horizon signals possibly related to impending earthquakes and a mechanism of seismo-atmospheric perturbations, *J. Atmos. Sol. Terr. Phys.*, *69*, 1057–1062.
- Kamogawa, M., and Y. Ohtsuki (1999), Plasmon model for origin of earthquake related electromagnetic wave noises, *Proc. Japan Acad.*, *75*, 186–189.
- Kittel, C. (1986), *Introduction to Solid State Physics*, 6th ed., John Wiley, New York.
- Kushida, Y., and R. Kushida (2002), Possibility of earthquake forecast by radio observations in the VHF band, *J. Atmos. Electricity*, *22*(3), 239–255.
- Moriya, T., T. Mogi, and M. Takada (2010), Anomalous pre-seismic transmission of VHF-band radio waves resulting from large earthquakes, and its statistical relationship to magnitude of impending earthquakes, *Geophys. J. Int.*, *180*, 858–870.
- Nagao, T., et al. (2002), Electromagnetic anomalies associated with 1995 Kobe earthquake, *J. Geodyn.*, *33*, 401–411.
- Press, W., S. Teukolsky, W. Vetterling, and B. Flannery (1992), *Flannery, Numerical Recipes in Fortran 77*, 2nd ed., chap. 3, pp. 99–122.
- Raether, H. (1977), *Surface Plasma Oscillations and Their Applications, Physics of Thin Films*, vol. 9, pp. 145–261, Academic Press, New York.
- Raether, H. (1988), *Surface Plasmons on Smooth and Rough Surfaces and on Gratings*, p. 5, Springer, Berlin.
- Scoville, J., J. Sornette, and F. Freund (2015), Paradox of peroxy defects and positive holes in rocks Part II: Outflow of electric currents from stressed rocks, *J. Asian Earth Sci.*, *114–2*, 338–351.

- Taflove, A., and S. C. Hagness (2005), *Computational Electrodynamics: The Finite-Difference Time-Domain Method*, 3rd ed., Artech House, Norwood, Mass.
- Takeuchi, A., and T. Nagao (2013), Activation of hole charge carriers and generation of electromotive force in gabbro blocks subjected to nonuniform loading, *J. Geophys. Res. Solid Earth*, *118*, 915–925, doi:10.1002/jgrb.50111.
- Uyeda, S., T. Nagao, and M. Kamogawa (2009), Short-term earthquake prediction: Current status of seismo-electromagnetics, *Tectonophysics*, *470*, 205–213.
- Yee, K. S. (1966), Numerical solution of initial boundary value problems involving Maxwell's equation in isotropic media, *IEEE Trans. Antennas Propag.*, *14*(5), 302–307.